





RESEARCH ARTICLE | DECEMBER 15 2022

# Nonlinear interactions of global instabilities in hypersonic laminar flow over a double cone

Special Collection: [Hypersonic Flow](#)

Jianhui Fan (范建辉) ; Jiaao Hao (郝佳傲)  ; Chih-Yung Wen (温志湧) 

 Check for updates

*Physics of Fluids* 34, 126108 (2022)  
<https://doi.org/10.1063/5.0130901>

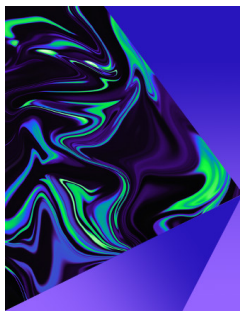


View  
Online



Export  
Citation

CrossMark



## Physics of Fluids

Special Topic:  
Selected Papers from the 2023 Non-Newtonian  
Fluid Mechanics Symposium in China

**Submit Today**

# Nonlinear interactions of global instabilities in hypersonic laminar flow over a double cone

Cite as: Phys. Fluids **34**, 126108 (2022); doi: [10.1063/5.0130901](https://doi.org/10.1063/5.0130901)

Submitted: 16 October 2022 · Accepted: 1 December 2022 ·

Published Online: 15 December 2022






View Online



Export Citation



CrossMark

Jianhui Fan (范建辉), , Jiaao Hao (郝佳傲),  <sup>a)</sup> and Chih-Yung Wen (温志湧) 

## AFFILIATIONS

Department of Aeronautical and Aviation Engineering, The Hong Kong Polytechnic University, Kowloon, Hong Kong

Note: This paper is part of the special topic, Hypersonic Flow.

<sup>a)</sup> Author to whom correspondence should be addressed: [jiaao.hao@polyu.edu.hk](mailto:jiaao.hao@polyu.edu.hk)

## ABSTRACT

Hypersonic laminar flow over a canonical 25–55° double cone is studied using computational fluid dynamics, bispectrum analysis, and dynamic mode decomposition (DMD) with a freestream Mach number of 11.5 and unit Reynolds number of  $1.6 \times 10^5 \text{ m}^{-1}$ . The present study focuses on the evolution and nonlinear behavior of perturbation modes in the flow. The presence of the perturbation modes is first described in detail through the results of direct numerical simulation. The results of high-order spectrum analysis (bispectrum) then reveal complex nonlinear interactions in the flow. By examining the evolution of such interactions, the frequency broadening phenomenon of the fully saturated flow is explained, and the unsteady dynamics of the fully saturated flow are recognized to be caused by the nonlinear saturation of linear instability in the flow. This causality is further confirmed by the DMD results of the Stanton number near the reattachment region. The origins and dynamics of unsteady saturated flow in the hypersonic laminar flow are, therefore, demonstrated.

Published under an exclusive license by AIP Publishing. <https://doi.org/10.1063/5.0130901>

## I. INTRODUCTION

Hypersonic flow over a double cone is one of the typical flows of shock-wave/boundary-layer interaction (SBLI).<sup>1</sup> The flow takes advantage of strong interaction and has no finite-span effects compared to its two-dimensional counterpart (i.e., a double wedge). It has been, therefore, extensively selected to study shock-induced separation.

Flow unsteadiness in SBLI is one of the significant features in hypersonic laminar flow over a double cone.<sup>2–5</sup> Different physical mechanisms can account for the unsteadiness. One of the possible mechanisms is that the unsteadiness of major shock structures is an inviscid phenomenon consistent with the pulsation mode in supersonic spiked-body flow.<sup>6</sup> In addition, the Kelvin–Helmholtz instability in the shear layer, which has dominant frequencies of 45–70 kHz, was reported by Tumuklu *et al.*<sup>7</sup> Additionally, there is one plausible mechanism that is related to self-sustained global instability for separated flows.<sup>8</sup> The mechanism is evident in numerical studies of hypersonic compression-ramp flows,<sup>9–12</sup> oblique shock-wave/laminar boundary-layer interaction,<sup>13,14</sup> hypersonic double wedge flow,<sup>15,16</sup> and hypersonic double cone flow.<sup>17</sup> For example, Hao *et al.*<sup>17</sup> performed a global stability analysis (GSA) of hypersonic flow over a 25–55° double cone with various Reynolds numbers and a direct numerical simulation for the highest Reynolds numbers. The authors identified that the development of perturbations in the early stage of flow evolution is due to

the intrinsic global instability, which is suggested by a consistent linear-growth rate between the most unstable global mode and the temporal direct numerical simulation (DNS) history of the azimuthal velocity.

However, the dynamics of flow unsteadiness in the linear-growth stage are not necessarily the same as those in the fully saturated flow.<sup>18</sup> The mechanism that gives rise to the unsteady dynamics of saturated flow is still unclear. There may be two possible sources contributing to the unsteady dynamics. When there is only one global unstable stationary mode revealed by the GSA, as indicated by the study of oblique SBLI flow,<sup>13</sup> the flow is three-dimensional and stationary in the linear-growth stage. Such three-dimensional stationary flow then evolves with the emergence of secondary instability in a transitional stage, leading the flow toward an unsteady saturated stage. When there are multiple global unstable modes (stationary or oscillating) revealed by the GSA, as indicated by the study of compression-ramp flow,<sup>9</sup> although the flow in the linear-growth stage is primarily three-dimensional and stationary, the unsteady dynamics of oscillating modes appear significant in the late linear-growth stage. Such unsteady features contributed by the oscillating modes may also be a potential source to determine the unsteady behavior when the flow becomes saturated. In both scenarios, the onset of the unsteady dynamics of flows almost begins at the commencement of a transitional stage. At the

transitional stage, the presence of multiple perturbation modes has been reported in many works in the literature. Robinet<sup>13</sup> observed that primary global instability and secondary instability are simultaneously present with nondimensional flow structure wavelengths of 0.8 and 0.4, respectively. By analyzing the power spectrum density, Cao *et al.*<sup>9</sup> observed that the wavelengths of multiple modes and the wavelength of the second harmonic of the most unstable stationary mode coexist in the flow field. Recently, Cao *et al.*<sup>11</sup> studied another hypersonic compression-ramp flow with a Reynolds number that was approximately double that of the previous one. The presence of multiple modes is also observed at the transitional stage. In addition, they found a second harmonic mode after the linear-growth stage by DNS results, which features a doubled wavenumber of the most unstable global mode revealed by the GSA. Thus, investigations of the nonlinear behaviors of these multiple perturbation modes can help to clarify the unsteady dynamics of the saturated flow.

The present study is an extension of Hao *et al.*,<sup>17</sup> of which some questions remain to be answered. For example, before the flow evolves to the fully saturated stage, there is a period of a transitional stage. How much and in what way can this transitional stage affect the flow dynamics at the fully saturated stage? In addition, our previous GSA results revealed multiple modes; however, only the most unstable stationary mode was discussed and compared with the DNS results in the linear-growth stage. How do the other modes contribute to the flow evolution and interact with each other nonlinearly? To answer these questions, a bispectrum technique and dynamics mode decomposition (DMD) are applied to the DNS data.

The following content of this paper is organized as follows. The flow configuration and numerical setup are described in Sec. II. In Sec. III, the evolution of perturbation modes in different stages is discussed by using DNS and DMD techniques, and the nonlinear behavior of these perturbation modes is investigated by a high-order spectrum analysis (bispectrum). Conclusions are given in Sec. IV.

## II. FLOW CONFIGURATION AND NUMERICAL SETUP

### A. Direct numerical simulation

The DNS has previously been reported by Hao *et al.*<sup>17</sup> An overview of the simulation methodology and setup is provided here. Further details may be found in the study by Hao *et al.*<sup>17</sup>

Figure 1 depicts the experimental model that was tested in the LENS I reflected shock tunnel and LENS XX expansion tunnel at the Calspan-University of Buffalo Research Center. Surface pressure and heat flux measurements<sup>19,20</sup> were conducted in the hypersonic flow regime with relatively low Reynolds numbers to maintain laminar flow. Special emphasis was given to the high-enthalpy effects. The 25–55° double cone features a sharp tip and two conical sections of equal length ( $L = 0.1016$  m). The coordinate system is created with the origin at the nose, the  $x$  direction is along the cone axis, the  $y$  direction is perpendicular to the axis, and the  $z$  direction satisfies the right-hand rule. Note that the direction of velocity components  $u, v, w$ , are parallel with the direction of  $x, y, z$ , respectively. In addition, the polar angle  $\theta$  is defined by  $\theta = \arccos(y/r)$ , where  $r = \sqrt{y^2 + z^2}$  and  $y > 0$  in the present study. The length of the conical section  $L$  is used as the characteristic length of the flow. The 3D computational grid is constructed by rotating a base grid ( $750 \times 350$ ) around the axis over an angle of  $72^\circ$  to make the DNS affordable. This azimuthal domain extent is also chosen because the corresponding critical wavenumbers

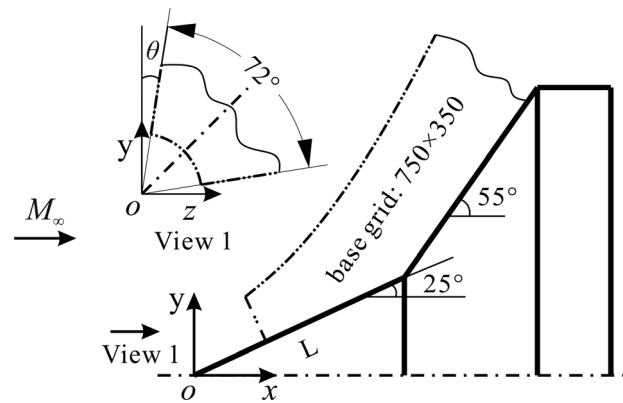


FIG. 1. Schematic of the double cone configuration.

( $m$ ) of modes obtained by the GSA are close to integer multiples of 5 (described in Sec. III). Note that information on the grid independence study has been reported in the previous work.<sup>17</sup>

An in-house multiblock parallel finite-volume solver called PHAROS, which has been successfully applied in many studies,<sup>21–26</sup> is employed for the simulation. An axisymmetric simulation of the present flow is first calculated to obtain a base-flow solution. Then, the initial flow field is constructed by duplicating the base-flow solution in the azimuthal direction. No external or internal disturbances are introduced in the present flow. The three-dimensional simulation is calculated with the following numerical schemes. The inviscid fluxes are computed by the advection upstream splitting method<sup>27</sup> and reconstructed by the monotone upstream-centered schemes for conservation law reconstruction.<sup>28</sup> The viscous fluxes are calculated by applying a second-order central difference. A second-order implicit scheme<sup>29</sup> is employed for time marching.

One of the double cone experiments<sup>30</sup> conducted in the LENS I tunnel (run 35) is considered in the present study. The freestream conditions are  $Re_\infty = 1.6 \times 10^5 \text{ m}^{-1}$ ,  $M_\infty = 11.5$ ,  $T_\infty = 138.9 \text{ K}$ ,  $\rho_\infty = 5.515 \times 10^{-4} \text{ kg/m}^3$ , and  $u_\infty = 2713 \text{ m/s}$ . The air is calorically perfect, with a constant specific heat ratio of 1.4 due to its low total enthalpy. The boundary conditions are given as follows: The profile from the corresponding axisymmetric solution is extracted to provide the inlet boundary conditions at the same streamwise station. The azimuthal boundaries are set as periodic boundary conditions. Simple extrapolation is used to determine the outflow boundary condition. The model surface is assumed to be no-slip, and the wall temperature is fixed at  $T_w = 300 \text{ K}$ . The physical time step of the simulation is set as 20 ns. The simulation is conducted for a total of 14 ms ( $tu_\infty/L = 374$ ) of physical time to obtain a fully saturated flow and capture enough periods of low-frequency unsteadiness. The sampling frequency is set to 0.5 MHz for data analysis.

A pseudo-schlieren image of the base flow is depicted in Fig. 2 to provide a basic picture of the flow. Figure 3 shows typical contours of surface Stanton number and density gradient magnitude by the DNS results at  $tu_\infty/L = 55, 125, \text{ and } 347$ . These three instants are intentionally selected to present flow structures in three main stages (defined in Sec. III) of flow evolution, which are linear-growth stage, transitional stage, and fully saturated stage. The surface Stanton number ( $St$ ) is defined by

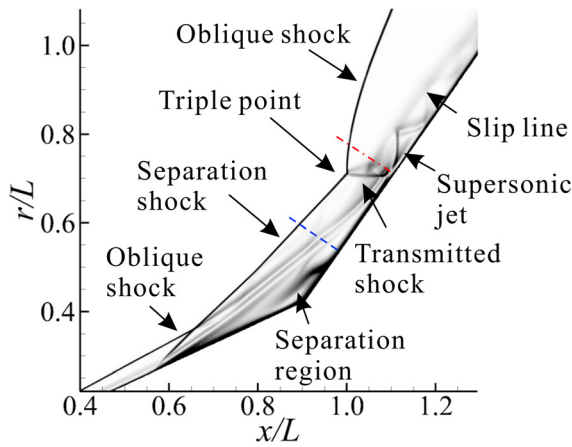


FIG. 2. Contours of the density gradient magnitude of the base flow. The blue dashed line and the red dashed-dotted line indicate the streamwise stations of  $x/L = 0.98$  and  $1.10$ , respectively.

$$St = \frac{q_w}{0.5\rho_\infty u_\infty^3}, \tag{1}$$

where  $q_w$  is the surface heat flux. The flow shows significant three-dimensionality, which is evidenced by the unsteady separation bubbles, and separation/reattachment lines. A more detailed three dimensional depiction of the present flow is presented in our previous work.<sup>17</sup>

$$Q_1^{N-1} = \underbrace{[\phi_1, \phi_2, \dots, \phi_{N-1}]}_\phi \begin{bmatrix} \alpha_1 & & & \\ & \alpha_2 & & \\ & & \ddots & \\ & & & \alpha_{N-1} \end{bmatrix} \tag{2}$$

$D_x = \text{diag}\{\alpha\}$

$$\times \underbrace{\begin{bmatrix} 1 & \mu_1 & \dots & \mu_1^{N-1} \\ 1 & \mu_2 & \dots & \mu_2^{N-1} \\ \vdots & \vdots & \ddots & \vdots \\ 1 & \mu_{N-1} & \dots & \mu_{N-1}^{N-1} \end{bmatrix}}_{V_{\text{and}}}$$

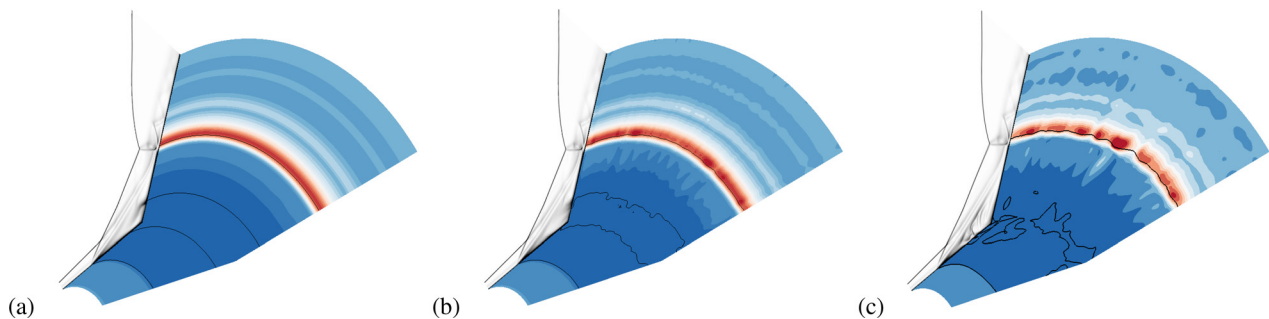


FIG. 3. Contours of surface Stanton number and density gradient magnitude by DNS results at (a)  $tu_\infty/L = 55$ , (b) 125, and (c) 347.  $St$  ranges from 0.02 to 0.14, and the black lines indicate isolines of zero-skin friction.

### B. Dynamic mode decomposition

In the present study, a frequency-orthogonal modal decomposition of the three-dimensional flow field is performed using dynamic mode decomposition (DMD) to separate the different dynamics from a broadband frequency spectrum. The method was first proposed by Schmid<sup>31</sup> to identify important information contained in a separated frequency component in an unsteady flow field. In summary, the original dynamic system will be reduced to a set of (reduced) modes, where each mode is linked with a single frequency behavior, the sum of which approximates the whole unsteady system.

Following the DMD methodology, the original dynamic system can be represented by Eq. (2), where  $\alpha_i$  is the amplitude of the  $i_{th}$  DMD mode ( $\phi_i$ ), and the Vandermonde matrix ( $V_{\text{and}}$ ) is the temporal evolution of the dynamic modes. Through the logarithmic mapping  $\lambda_i = \ln(\mu_i)/\Delta t$ , the eigenvalues  $\mu_i$  can be converted into a complex stability plane. The dynamic information about the growth rate  $\sigma_i$  and angular frequency  $\omega_i$  of a specific DMD mode is then computed by

$$\sigma_i = \text{RE}(\lambda_i) = \ln |\mu_i|/\Delta t, \tag{3}$$

$$\omega_i = \text{IM}(\lambda_i) = \text{Arg}(\mu_i)/\Delta t. \tag{4}$$

### C. Bispectrum

The nonlinear behaviors in the flow are studied using a bispectrum analysis.<sup>32</sup> For a continuous time-varying signal  $q(t)$ , the bispectrum is defined by

$$B(f_1, f_2) = \lim_{T \rightarrow \infty} \frac{1}{T} E[Q(f_1)Q(f_2)Q^c(f_1 + f_2)], \tag{5}$$

where  $T$  is the temporal duration of the signal  $q(t)$ ,  $Q(t)$  is the Fourier transform of  $q(t)$ , the superscript  $c$  represents the conjugate transpose, and  $E[\cdot]$  is the expectation operator. The bispectrum can indicate the presence of interactions between a group of signal components at  $f_1, f_2$ , and  $f_1 + f_2$  obtained from a time-varying signal. For example, a quadratic nonlinearity is the production of a harmonic by a wave with a frequency  $f_0$  coupling with itself,  $f_0 + f_0 \rightarrow 2f_0$ . Note that the bispectrum can only indicate the presence of quadratic nonlinearity and is not effective in detecting other forms (e.g., cubic nonlinear interactions).

### III. PERTURBATION MODES IN THE FLOW

In this section, we identify the perturbation modes for hypersonic laminar flow over a double cone. An azimuthal velocity at a given

streamwise station of  $x/L = 0.98$  (the blue dashed line in Fig. 2) is used to represent perturbation quantitatively. The velocity is defined by

$$A_w = \sqrt{\frac{1}{N_j N_k} \sum_{j=1}^{N_j} \sum_{k=1}^{N_k} \left( \frac{V_{azi}}{u_\infty} \right)^2}, \quad (6)$$

where  $V_{azi} = w \cos(\theta) - v \sin(\theta)$  and  $N_j$  and  $N_k$  are the numbers of grid cells in the radial and azimuthal directions, respectively. The temporal history of this velocity is shown in Fig. 4. By examining the features in the flow history, the whole simulation can be separated into three main stages. The linear-growth stage consists of a linear exponential growth section and a short period of the saturated section, which ranges from approximately  $tu_\infty/L = 5$  to 115. The second stage ( $tu_\infty/L = 115$  to 240) is a transitional process from the linear-growth state to the fully saturated stage. After a period of transition, a fully saturated flow is finally established from  $tu_\infty/L = 240$ .

### A. Perturbation modes in the linear-growth stage

Perturbation modes in the linear-growth stage can be revealed by a previous GSA,<sup>17</sup> as shown in Fig. 5. The figure presents the variations in the growth rates and the frequencies of the most unstable modes as a function of azimuthal wavenumber for the base flow. Modes 1–4 are the primary stationary mode, primary oscillatory mode, secondary stationary mode, and secondary oscillatory mode, respectively. The azimuthal wavenumbers for the most unstable modes 1–4 are 33, 30, 5, and 17, respectively, which are the critical wavenumbers in the present study. Additionally, the nondimensionalized oscillating frequency of the most unstable oscillating mode 2 at  $m = 33$  is approximately 0.2.

By comparing the GSA results and DNS results, we noted that although GSA modes are obtained based on a linearized Navier–Stokes equation,<sup>8</sup> a similar perturbation mode can also be observed from the flow field by DNS. Thus, in the following content, if one mode by DNS is almost identical to the mode revealed in the GSA, the mode will be named the same mode as in the GSA for convenience. Figure 6 shows

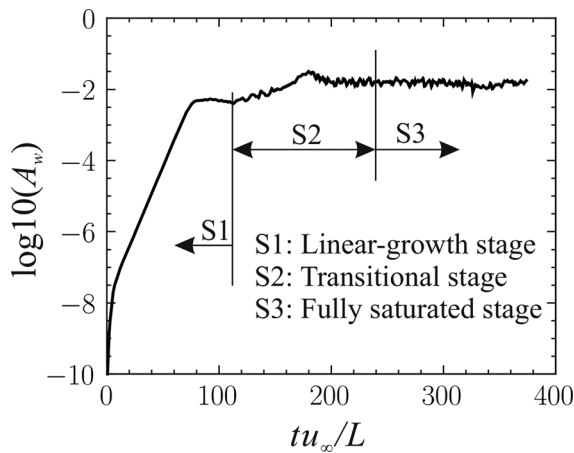


FIG. 4. Temporal history of the root mean square of the azimuthal velocity at  $x/L = 0.98$ .

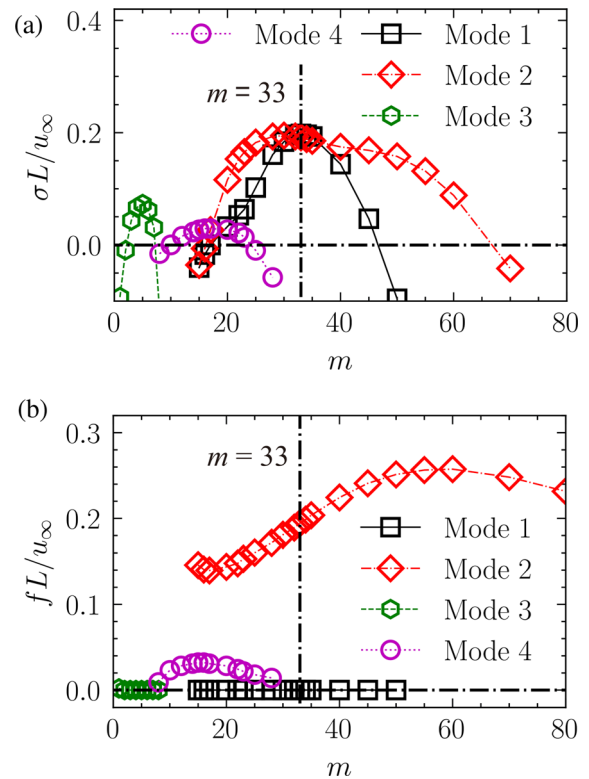
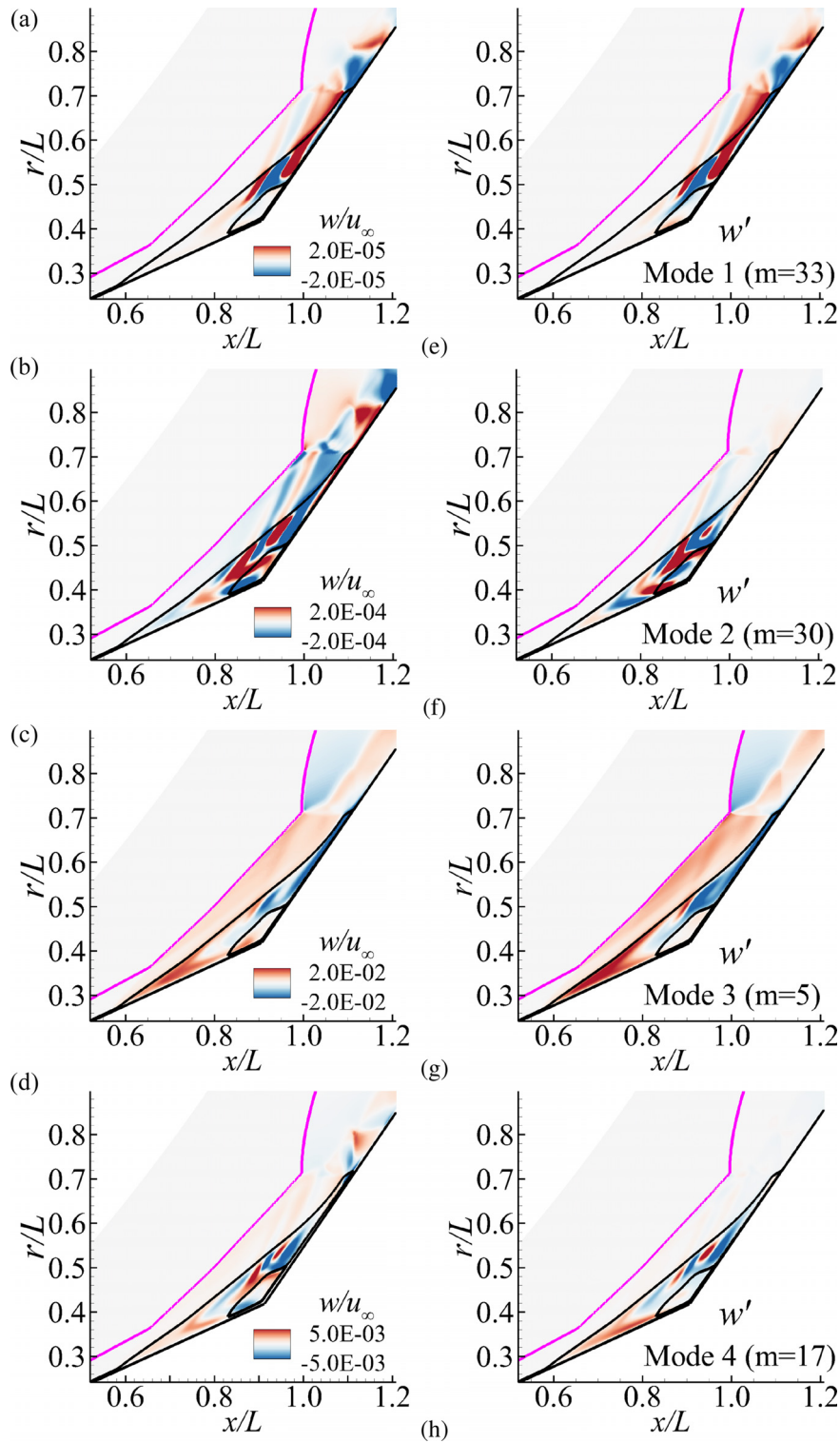


FIG. 5. Variations in (a) the growth rates and (b) the frequencies of the most unstable modes as a function of azimuthal wavenumber for the base flow.

the four contours of azimuthal velocity within the linear-growth stages by DNS [Figs. 6(a)–6(d)] and GSA results [Figs. 6(e)–6(h) corresponding to modes 1–4]. These four typical DNS contours share high similarities with the perturbation modes of the GSA.

By examining the evolution of the flow field and features shown in Figs. 4 and 6, the development of perturbation modes during the early stage of flow evolution can be described as follows. After flow initialization, the perturbation in the flow grows linearly under stationary mode 1 at first. At the late linear stage, the perturbation grows with the oscillating mode 2 setting in. Meanwhile, a new perturbation mode occurs in the flow field, which is recognized as stationary mode 3. The emergence of mode 3 can also be seen in Fig. 7, which shows that the azimuthal wavenumber of coherence structures in the flow field evolves from roughly  $m = 30$  to 5. A similar phenomenon is also reported by Cao *et al.*<sup>10</sup> In their study, a new mode is identified after the linear-growth stage by flow patterns (spanwise velocity), which exhibit a wavenumber that is twice that of the linear-growth stage. Apart from the emergence of mode 3, mode 4 also becomes significant at the late linear-growth stage. As indicated in Fig. 8, the high energetic components in Fig. 8(a) feature critical wavenumbers of mode 1 and mode 2, whereas the high energetic components in Fig. 8(b) can also distribute in the low wavenumber region. The highly energetic spots with low wavenumbers in Fig. 8(b) suggest the emergence of a perturbation mode (mode 4) with a critical wavenumber of 15.



**FIG. 6.** Contours of the azimuthal velocity superimposed with shock locations and dividing streamlines by DNS at (a)  $tu_\infty/L = 55$ ,  $\theta = 42.5^\circ$ , (b)  $tu_\infty/L = 72$ ,  $\theta = 40.5^\circ$ , (c)  $tu_\infty/L = 115$ ,  $\theta = 30.0^\circ$ , and (d)  $tu_\infty/L = 100$ ,  $\theta = 13.5^\circ$ , and by the GSA at (e)  $m = 33$ , (f) 30, (g) 5, and (h) 17. The contour levels of the GSA modes are evenly spaced between  $\pm 0.1$  of the maximum  $|w'|$  for modes 1 and 2 and  $\pm 0.5$  of the maximum  $|w'|$  for modes 3 and 4.

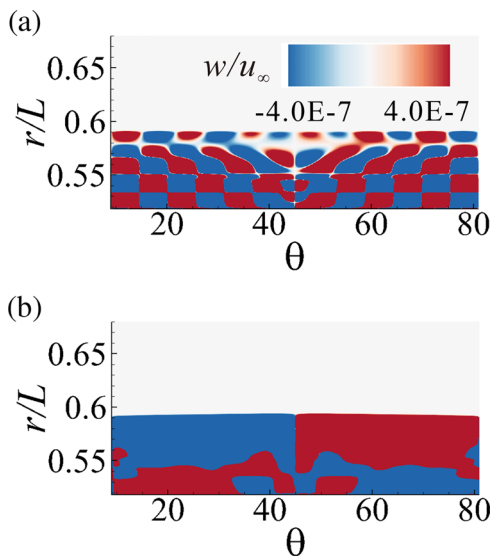


FIG. 7. Contours of the azimuthal velocity in wall-normal slices extracted at  $x/L = 0.98$  at (a)  $tu_\infty/L = 55$  and (b) 115.

**B. Perturbation modes in the transitional stage**

Perturbation modes in the transitional stage can be revealed by a DMD analysis in the present study. Our dataset for the following DMD analysis is constructed by snapshots of azimuthal velocity within the transitional stage ( $tu_\infty/L = 125\text{--}160$ ) at time step = 0.05 ms. The resultant number of snapshots is  $n = 24$  in this setup, and the resolved frequency can reach  $fL/u_\infty = 0.375$  with the minimum resolvable frequency of  $fL/u_\infty = 0.015$ . The setup is sufficient for the purpose of capturing critical modes from the DNS results, because increasing the sampling frequency resulted in additional similar perturbation modes. The computation domain for the modal analysis covers a range of  $0.4 < x/L < 1.4$  with the entire  $r/L$  range and  $\theta = 30^\circ$ . Note that the resultant DMD modes with a given  $\theta$  are an instantaneous representation of perturbation motions.

Figure 9 shows the eigenvalue spectrum of the DMD results for azimuthal velocity within the transitional stage. Six DMD modes are highlighted by colored symbols in the figure, and the modes are shown in Fig. 10 to represent typical modes within the resolved frequency. As can be seen in the figure, there is a stationary mode that is marked by

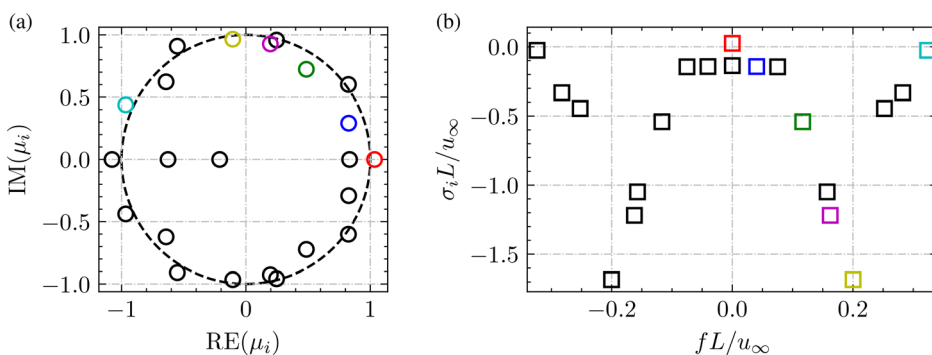


FIG. 9. (a) Spectrum of eigenvalues resulting from the DMD for azimuthal velocity within the transitional stage. (b) Growth rate of DMD modes with  $fL/u_\infty < 0.34$ . The colored circle symbols indicate the DMD modes in Fig. 10.

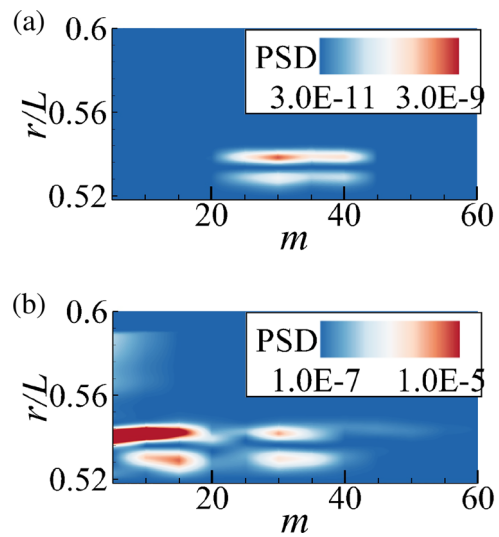
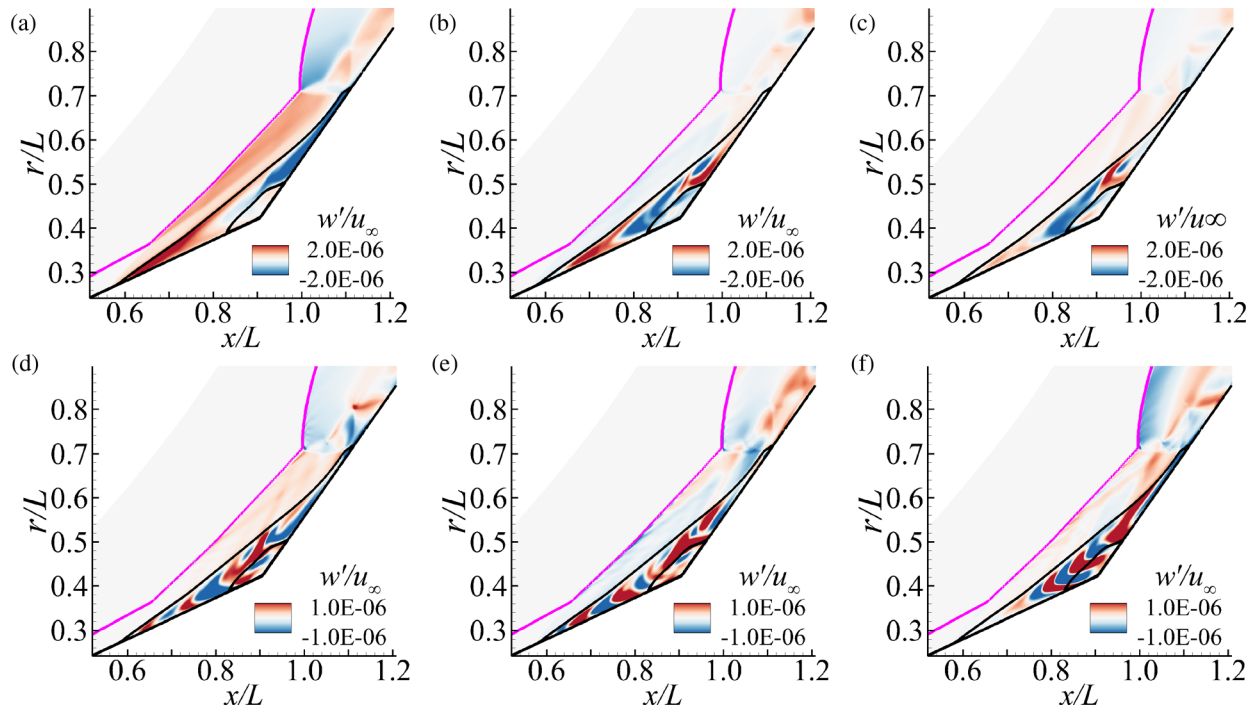


FIG. 8. PSD of the azimuthal velocity in wall-normal slices extracted at  $x/L = 0.98$  at (a)  $tu_\infty/L = 55$  and (b) 115.

the red symbol. By examining the real part of the DMD mode [shown in Fig. 10(a)], the DMD mode is roughly identical to both the DNS results [Fig. 6(c)] and mode 3 of the GSA. For oscillating modes with  $fL/u_\infty = 0.04$  and  $0.11$  [Figs. 10(b) and 10(c)], the modes share a similar structure as mode 4 revealed by the GSA. For oscillating mode with critical frequency close to  $0.2$  [Figs. 10(d)–10(f)], the modes show similar variations to mode 2 but with more pairs of repeating coherence structures in the upstream half of the separation region. For oscillating modes with high frequency [Fig. 10(g)], the entire separation region is almost occupied by the coherence structures, and it is found that the pairs of coherence structures within the separation bubble increase with increasing oscillating frequency. Note that the cause of the coherence structures is still unclear and awaits further investigation.

Figure 11 shows the difference in the spectra of the  $St$  signal before and after the transitional stage. Figure 11(a) shows the temporal history of the azimuthally averaged surface  $St$  signal at  $x/L = 1.10$  (the red dashed line in Fig. 2), and the corresponding power spectral densities (PSDs) for the linear-growth stage ( $tu_\infty/L = 5$  to 80) and the fully saturated stage ( $tu_\infty/L = 280\text{--}374$ ) are provided in Figs. 11(b)



**FIG. 10.** Real part of DMD modes showing contours of modal azimuthal velocity fluctuation superimposed with shock locations and dividing streamlines. The modes correspond to (a) the red symbol with  $fL/u_\infty = 0$ , (b) the blue symbol with  $fL/u_\infty = 0.04$ , (c) the green symbol with  $fL/u_\infty = 0.11$ , (d) the magenta symbol with  $fL/u_\infty = 0.16$ , (e) the yellow symbol with  $fL/u_\infty = 0.20$ , and (f) the cyan symbol with  $fL/u_\infty = 0.32$  in Fig. 9.

and 11(c), respectively. The PSD curves are obtained by applying Welch’s method<sup>33</sup> with two segments, a 50% overlap and a Hamming window. Before the transitional stage, there is a peak PSD located at  $fL/u_\infty \approx 0.2$ . As expected, this value is almost the same as the oscillating frequency of mode 2 predicted by the GSA. However, after the flow is saturated, the frequency of the peak PSD shifts toward  $fL/u_\infty = 0.1$ . Meanwhile, frequency broadening is also observed in the low-frequency region by comparing these two PSD curves. The generation of the discrepancies mentioned above can be accounted for the nonlinear behavior during the flow evolution. Thus, a higher-order spectrum analysis is applied to identify such nonlinear behavior features.

Figure 12 shows the bispectrum of the azimuthally averaged surface Stanton number signal at three different stages at  $x/L = 1.10$ . A peak at the bispectrum of a frequency pair  $(f_1, f_2)$  indicates that a quadratic interaction exists between modes at  $f_1$ ,  $f_2$ , and  $f_1 + f_2$ . Interactions between these frequencies may be  $f_1 + f_2 \rightarrow (f_1 + f_2)$  or  $(f_1 + f_2) - f_1 \rightarrow f_2$  or  $(f_1 + f_2) - f_2 \rightarrow f_1$ . The bispectrum cannot distinguish these sum or difference interactions by itself. Normally, with the help of contextual clues and supporting evidence, interactions can finally be determined. The fundamental frequency  $f_0$  is set as  $fL/u_\infty = 0.2$ , which is close to the oscillating frequency of mode 2 revealed by the GSA.

In Fig. 12(a), the bispectrum shows a peak at  $(0, 1)$ . Considering that the spectrum is obtained from the linear-growth stage, the zero frequency can be related to stationary mode 1, and  $f_0$  can be related to

the oscillating frequency of mode 2 revealed by the GSA. Thus, it is likely that this interaction represents  $0 + 1 \rightarrow 1$ . Around the region of peak  $(0, 1)$ , a high level of bispectrum magnitude ( $B$ ) is observed. As indicated by the presence of the  $St$  amplitude modulation shown in Fig. 12(a) and mode 2 in Fig. 11(b), these high values represent the interaction  $\varepsilon + 1 \rightarrow (\varepsilon + 1)$ , which should be one of the sources contributing to the spectral broadening depicted in Fig. 11. Here,  $\varepsilon$  stands for a small frequency deviation from the zero frequency, and in the present study, it can be a low frequency contributed by the amplitude modulation mentioned above. The origins of this modulation may be due to the typical oscillating mode 4 [Fig. 10(b)] with critical frequency  $fL/u_\infty < 0.04$ . Note that the  $St$  amplitude modulation arises from approximately  $tu_\infty/L = 55$ .

In Fig. 12(b), the nonlinearity becomes more significant during the transitional stage. The presence of self-interactions can be read from the bispectrum along a  $45^\circ$  line of the coordinate. Starting from the origins of the coordinate, there is an apparent peak located at  $(0, 0)$ . This interaction  $(0 + 0 \rightarrow 0)$  may be interpreted by the multi-stationary modes (modes 1 and 3 in Fig. 5). Evidence of this view is supplied by the difference between Figs. 12(a) and 12(b) at point  $(0, 0)$ , as mode 3 significantly appears after the linear-growth stage. The next significant peak along the  $45^\circ$  line is at point  $(1, 1)$ . This peak represents a self-interaction of the fundamental frequency. An interesting feature is the spectral support in the vicinity of the self-interaction, indicated by a dashed circle shown in the figure. Combined with another two bispectrum plots, this feature may be



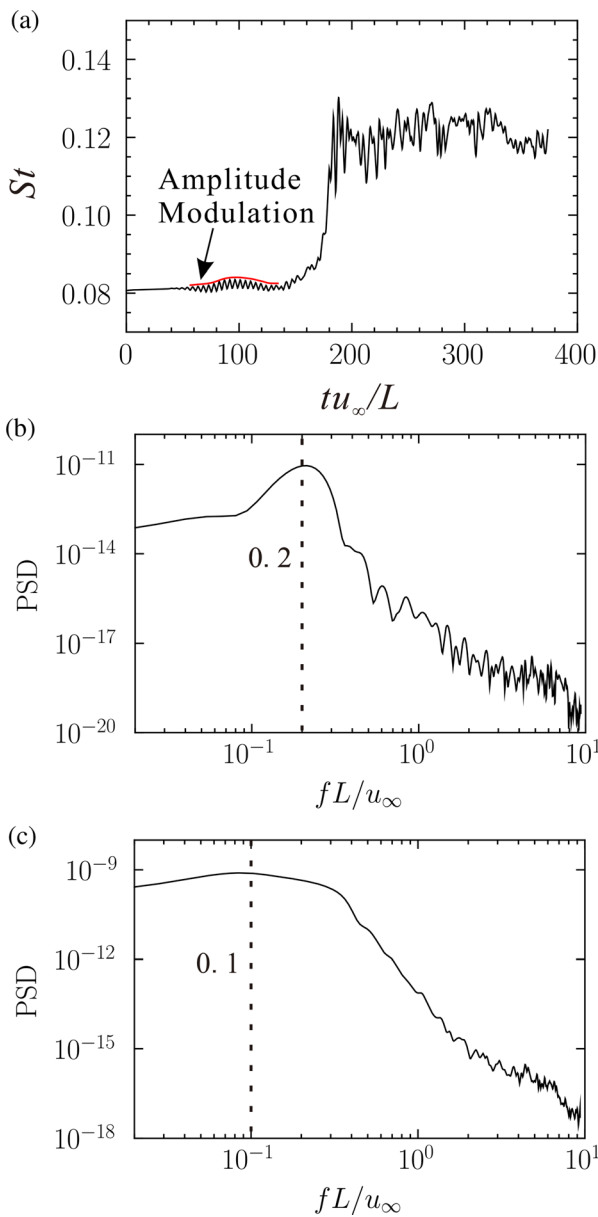


**FIG. 11.** (a) Temporal history of the azimuthally averaged surface  $St$  signal at  $x/L = 1.10$ , (b) the corresponding PSD of the  $St$  signal at the linear-growth stage ( $tu_\infty/L = 5$  to  $80$ ), and (c) the corresponding PSD of the  $St$  signal at the fully saturated stage ( $tu_\infty/L = 280$  to  $374$ ).

read as an interaction that occurs in the middle process of the generation of subharmonics. The interaction can be represented as  $(1 - \Delta + 1) - 1 \rightarrow (1 - \Delta)$ , where  $\Delta$  is a small deviation from the fundamental frequency. When  $\Delta$  is somewhere between 0 and  $1/2$ , we have the feature of Fig. 12(b) mentioned above. With the flow developed,  $\Delta$  evolves and reaches  $1/2$ . A peak is, therefore, obtained at the point  $(1, 1/2)$ , which indicates an interaction of  $(1/2 + 1) - 1 \rightarrow 1/2$ . Note that the subharmonic generation may account for the shift in the peak frequency, as shown in Fig. 11.

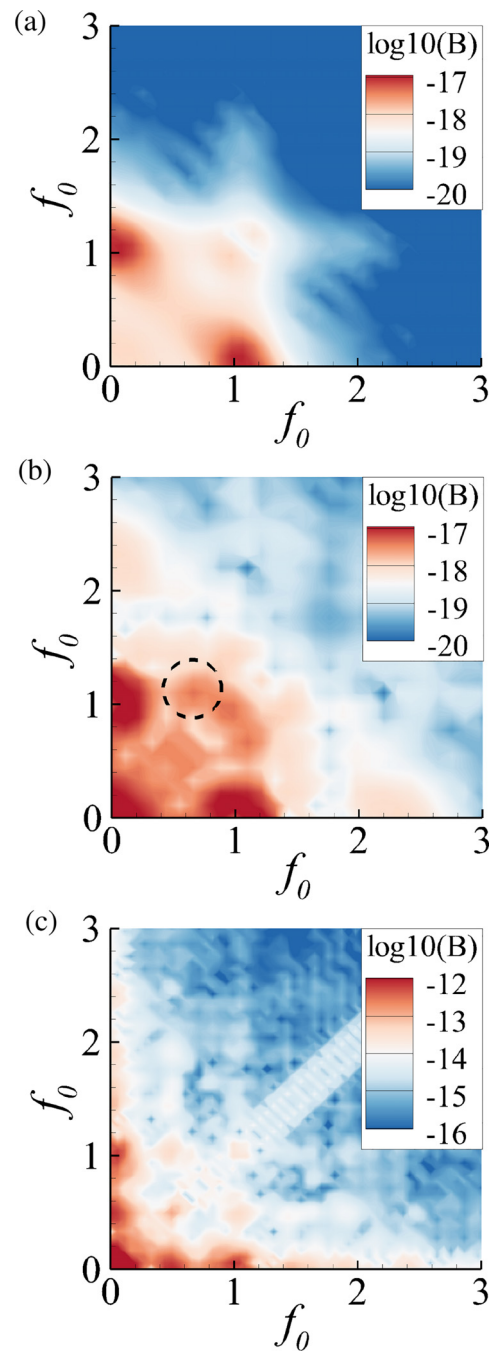


**FIG. 12.** Bispectrum of the azimuthally averaged surface Stanton number signal at the (a) linear-growth stage ( $tu_\infty/L = 5$  to  $80$ ), (b) transitional stage ( $tu_\infty/L = 125$  to  $160$ ), and (c) fully saturated stage ( $tu_\infty/L = 280$  to  $374$ ). The axes are normalized by the fundamental frequency  $f_0$ .

In Fig. 12(c), the resultant subharmonic then self-interacts as indicated by the local peak at  $(1/2, 1/2)$  and interacts with stationary modes as indicated by the local peak at  $(1/2, 0)$ . In addition, along the axes, there are three significant spots located around  $(0, 0)$ ,  $(1/2, 0)$ ,

and  $(1, 0)$ . These spots indicated the interactions of  $\varepsilon + \varepsilon \rightarrow (\varepsilon + \varepsilon)$ ,  $\varepsilon + 1/2 \rightarrow (\varepsilon + 1/2)$ , and  $\varepsilon + 1 \rightarrow (\varepsilon + 1)$ , which contribute to the frequency broadening as shown in Fig. 11. Overall, nonlinear features in the bispectrum of the fully saturated flow can be well explained by the modes revealed by linear instability theory. Thus, it is reasonable to believe that the unsteadiness of the saturated flow is due to the nonlinear interaction of critical perturbation modes in the present flow.

### C. Perturbation modes in the fully saturated stage

In Sec. III B, we provide a view that the unsteady dynamics of saturated flow are due to the nonlinear interaction of critical perturbation modes in the present flow. In this section, a detailed analysis based on the DMD method is conducted to further confirm this view by examining the unsteady dynamics of thermal streaks.

Our database for the wall surface DMD analysis is constructed by  $n = 1700$  snapshots of  $St$  with a time step of  $0.002 \text{ ms}$  ( $tu_\infty/L = 280$  to  $374$ ). The current setting of the database results in a frequency resolution of  $5.5 \times 10^{-3} < fL/u_\infty < 9.3$ , which is sufficient to resolve the low-frequency phenomenon in the present study. The computation domain for the DMD covers the range  $1.0 < x/L < 1.35$  and  $9^\circ < \theta < 81^\circ$ , which includes the dynamically interesting interaction region (reattachment region).

Figure 13(a) illustrates the spectrum of eigenvalues resulting from the DMD algorithm. As the processed input data are real values, the resultant modes are in the form of complex conjugate pairs, resulting in a symmetrical spectrum. In addition, as the saturated flow is a quasi-steady flow, it is expected that almost all eigenvalues lie on the unit circle  $|\mu_i| = 1$ .<sup>34</sup> The blue “diamond” symbols shown in the figure are a subset of dynamically important modes ( $N_{sub} = 37$ ) that have been selected by the sparsity promoting DMD (SPDMD) algorithm. This algorithm was developed by Jovanović *et al.*<sup>35</sup> for the purpose of automatically selecting dynamically important modes from all standard DMD modes. It does not simply select DMD modes according to their magnitude but identifies the modes that have the greatest influence on the complete snapshot sequence. Figure 13(b) presents the subset ( $N_{sub} = 37$  and  $9$ ) of dynamically important modes selected by the SPDMD. The selected subset modes are distributed mainly in the low-frequency region and present a broadband low-frequency feature. This is consistent with the feature of the PSD curve shown in Fig. 11 (c). Among these modes, there are four modes (marked as red diamonds) selected by the SPDMD with  $N_{sub} = 9$ . The

nondimensionalized frequencies for these four modes are  $fL/u_\infty = 0.039, 0.080, 0.121, \text{ and } 0.168$ , respectively.

Figure 14 shows the real part of the four modes ( $N_{sub} = 9$ ) of the Stanton number at a given frequency component, which is defined by  $St'$  in the present study. As can be seen in the image, a high level of surface Stanton number fluctuation is found downstream of the reattachment lines. Each mode typically has flow patterns (red and blue spots) as indicated by the dashed circle in Fig. 14(a). These flow patterns describe an oscillation of the thermal streak and account for the corrugate reattachment line, as observed in previous work.<sup>17</sup> The PSD contours of the four modes also suggest that unsteady dynamics of the saturated flow are related to the linear modes mentioned in Sec. III A. As shown in Fig. 15, these spectra show a high PSD magnitude downstream of the reattachment line with wavenumbers located at some critical values (such as  $m = 5, 30, 35$  and their couplings). The saturated flow has interactions between different linear modes, leading to these spectra containing high energy content around these critical wavenumbers.

An animation is also reconstructed by superimposing the mean flow field with these four DMD modes to further study the three-dimensionality of the present flow. The reconstruction is described as follows.<sup>36</sup> The reconstructed real-value flow variable consists of two parts. The first part is  $\phi_m$ , which represents the mean mode. The second part is perturbations contributed from each mode, which is expressed as  $\sum_i^N (a_f \cdot \text{RE}\{\alpha_{i,opt} \phi_i e^{i\omega_i t + \sigma_i t} + cc\})$ . Here, “cc” indicates the contribution of the complex conjugate of  $\phi_i$ , and  $a_f$  is an optional amplification factor. Since the present flow is a quasi-steady flow, the growth rate ( $\sigma_i$ ) of each mode is nearly zero and is neglected during the reconstruction.<sup>37</sup> The animation shows contours of the surface Stanton number in the range  $St = [0.02, 0.14]$  at eight equally spaced phase angles ( $\omega_i t$ ), which is  $j\pi/4$  ( $j = 0, \dots, 7$ ).

Figure 16(a) (Multimedia view) shows the reconstructed animation of surface Stanton number by DMD, and Fig. 16(b) shows the animation of surface Stanton number by DNS. In the reconstructed animation, the dynamics of the thermal streaks near flow reattachment are well demonstrated. The heat flux peak and valley appear alternatively along the azimuthal direction, and the number of these structures is mainly determined by the critical wavenumber of the linear modes. These heat flux features form as a whole and exhibit another oscillatory motion along the azimuthal direction with an azimuthal wavenumber of 5. By comparing the  $St$  distribution in these two animations, overall, unsteady motions shown in the DMD animation can basically reproduce the motions shown in the DNS animation. This

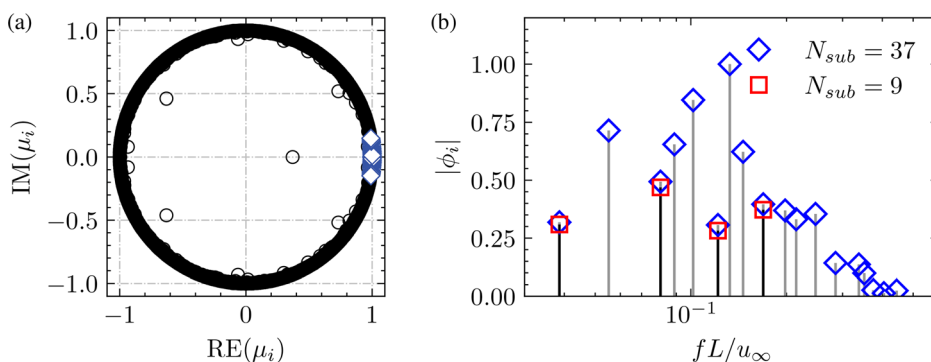


FIG. 13. (a) Spectrum of eigenvalues resulting from the DMD for the Stanton number. (b) Magnitude of DMD modes (normalized by the max magnitude in the plot). Blue diamonds indicate a subset of SPDMD with  $N_{sub} = 37$  and red diamonds indicate a subset of SPDMD with  $N_{sub} = 9$ .

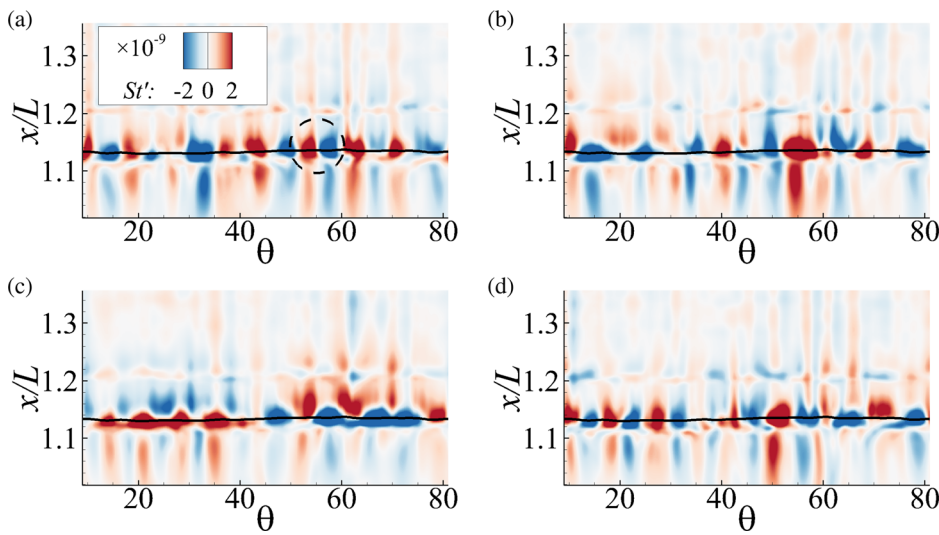


FIG. 14. (a) Real part of DMD modes showing contours of modal Stanton number fluctuation with  $1.0 < x/L < 1.35$  and  $9^\circ < \theta < 81^\circ$ . The solid line denotes the averaged zero-skin friction. (a) Mode  $\phi 1$  ( $fl/u_\infty = 0.039$ ), (b) mode  $\phi 2$  ( $fl/u_\infty = 0.080$ ), (c) mode  $\phi 3$  ( $fl/u_\infty = 0.121$ ), and (d) mode  $\phi 4$  ( $fl/u_\infty = 0.168$ ).

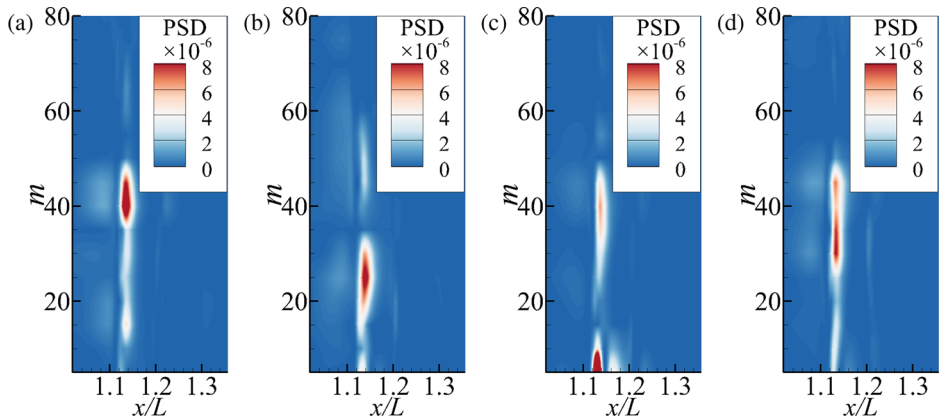


FIG. 15. Power spectral densities of the modes are shown in Fig. 16. (a) Mode  $\phi 1$  ( $fl/u_\infty = 0.039$ ), (b) mode  $\phi 2$  ( $fl/u_\infty = 0.080$ ), (c) mode  $\phi 3$  ( $fl/u_\infty = 0.121$ ), and (d) mode  $\phi 4$  ( $fl/u_\infty = 0.168$ ).

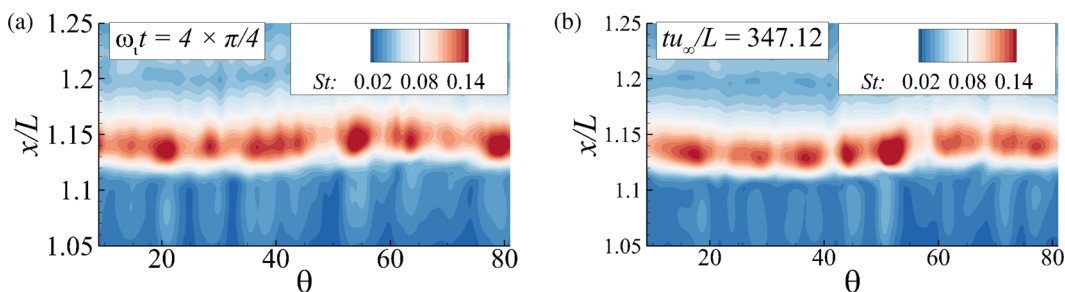


FIG. 16. (a) Reconstructed animation of surface Stanton number by DMD. (b) Animation of surface Stanton number by DNS. Multimedia views: <https://doi.org/10.1063/5.0130901.1>; <https://doi.org/10.1063/5.0130901.2>

suggests that the dynamics of the thermal streaks in the DNS are due to the nonlinear saturation of critical linear modes in the flow. Additionally, the similarity may also suggest that critical design parameters (e.g., wall heat flux) can be well predicted by applying a reduced order model in the SBLI flow, leading to significant computational cost savings.

IV. CONCLUSIONS

Hypersonic laminar flow over a canonical 25–55° double cone is studied using computational fluid dynamics, bispectrum analysis, and dynamic mode decomposition with a freestream Mach number of 11.5 and unit Reynolds number of  $1.6 \times 10^5 \text{ m}^{-1}$ . The study is conducted to clarify the unsteady dynamics of fully saturated flow by

11 January 2024 03:05:03

investigating the nonlinear behavior of perturbation modes at the transitional stage. The significant findings are listed as follows.

The presence of the critical perturbation modes is first identified by the DNS results. Apart from the most unstable stationary mode and the most unstable oscillating mode, which are significant in the linear-growth stage, there are new modes arising in the flow after the linear-growth stage. These critical multiple perturbation modes interact, and their interactions are studied using a bispectrum analysis. The bispectrum results then explain the generation of the typical frequency broadening phenomenon and indicate that the unsteady dynamics of the saturated flow are caused by the nonlinear saturation of the linear mode in the flow. This causality is further confirmed by the DMD analysis for the surface heat flux.

The findings in the present work demonstrate how perturbation modes evolve, interact with each other, and finally contribute to the unsteady dynamics of the fully saturated flow, providing a better understanding of the formation and dynamics of the unsteady saturated flow under the condition of free external perturbation and global instability. It is worth noting that such unsteady dynamics will be essentially different if the flow conditions change. Consider the dynamics of thermal streaks as an example for the following discussion. If flow conditions are globally stable and no perturbations are introduced, the reattachment line will be a straight line, and there will be no thermal streaks.<sup>14,16</sup> If flow conditions are globally stable and perturbations are introduced, the dynamics of the thermal streaks will be determined by the perturbations, and the perturbations are amplified by a convective mechanism, as indicated by Dwivedi *et al.*<sup>38–41</sup> and Bugeat *et al.*<sup>42,43</sup> If flow conditions are globally unstable and no perturbations are introduced, the dynamics of the thermal streaks will behave as we present in the present study. However, if flow conditions are globally unstable and perturbations are introduced, the dynamics of the thermal streaks are still not fully understood, and it is likely to be determined by both convective and intrinsic mechanisms. Most shock-wave/turbulent boundary-layer (STBLI) interactions with large separation belong to this category,<sup>44–50</sup> as the turbulent boundary layer continuously introduces perturbations into the separated flow. The convective/intrinsic mechanisms may also be a potential way to explain the other dynamics that occurred in STBLI flows (e.g., low-frequency motions of separation bubbles), which is very worthwhile for future study. Thus, the findings in the present study also provide a preliminary understanding of the study on the dynamics in STBLI flows.

## ACKNOWLEDGMENTS

This work was supported by the Hong Kong Research Grants Council (No. 15206519).

## AUTHOR DECLARATIONS

### Conflict of Interest

The authors have no conflicts to disclose.

## Author Contributions

**Jianhui Fan:** Data curation (lead); Formal analysis (lead); Investigation (lead); Methodology (lead); Writing – original draft (lead). **Jiaao Hao:** Conceptualization (supporting); Funding

acquisition (supporting); Supervision (supporting); Writing – review & editing (supporting). **Chih-Yung Wen:** Conceptualization (supporting); Funding acquisition (supporting); Supervision (supporting); Writing – review & editing (supporting).

## DATA AVAILABILITY

The data that support the findings of this study are available from the corresponding author upon reasonable request.

## REFERENCES

- H. Babinsky and J. K. Harvey, *Shock Wave-Boundary-Layer Interactions* (Cambridge University Press, 2011).
- J. Hao, J. Wang, and C. Lee, “Numerical simulation of high-enthalpy double-cone flows,” *AIAA J.* **55**(7), 2471–2475 (2017).
- O. Tumuklu, D. A. Levin, and V. Theofilis, “Investigation of unsteady, hypersonic, laminar separated flows over a double cone geometry using a kinetic approach,” *Phys. Fluids* **30**, 046103 (2018).
- G. Kumar and A. De, “Modes of unsteadiness in shock wave and separation region interaction in hypersonic flow over a double wedge geometry,” *Phys. Fluids* **33**, 076107 (2021).
- G. Kumar and A. De, “Role of corner flow separation in unsteady dynamics of hypersonic flow over a double wedge geometry,” *Phys. Fluids* **33**, 036109 (2021).
- H. Hornung, R. J. Gollan, and P. A. Jacobs, “Unsteadiness boundaries in supersonic flow over double cones,” *J. Fluid Mech.* **916**, A5 (2021).
- O. Tumuklu, V. Theofilis, and D. A. Levin, “On the unsteadiness of shock-laminar boundary layer interactions of hypersonic flows over a double cone,” *Phys. Fluids* **30**, 106111 (2018).
- V. Theofilis, “Global linear instability,” *Annu. Rev. Fluid Mech.* **43**, 319–352 (2011).
- S. Cao, J. Hao, I. Klioutchnikov, H. Olivier, K. A. Heufer, and C. Wen, “Leading-edge bluntness effects on hypersonic three-dimensional flows over a compression ramp,” *J. Fluid Mech.* **923**, A27 (2021).
- S. Cao, J. Hao, I. Klioutchnikov, H. Olivier, and C. Wen, “Unsteady effects in a hypersonic compression ramp flow with laminar separation,” *J. Fluid Mech.* **912**, A3 (2021).
- S. Cao, J. Hao, I. Klioutchnikov, C. Wen, H. Olivier, and K. A. Heufer, “Transition to turbulence in hypersonic flow over a compression ramp due to intrinsic instability,” *J. Fluid Mech.* **941**, A8 (2022).
- J. Hao, S. Cao, C. Wen, and H. Olivier, “Occurrence of global instability in hypersonic compression corner flow,” *J. Fluid Mech.* **919**, A4 (2021).
- J. C. Robinet, “Bifurcations in shock-wave/laminar-boundary-layer interaction: Global instability approach,” *J. Fluid Mech.* **579**, 85–112 (2007).
- N. Hildebrand, A. Dwivedi, J. W. Nichols, M. R. Jovanovi, and G. V. Candler, “Simulation and stability analysis of oblique shock-wave/boundary-layer interactions at Mach 5.92,” *Phys. Rev. Fluids* **3**, 013906 (2018).
- S. Sawant, V. Theofilis, and D. Levin, “On the synchronisation of three-dimensional shock layer and laminar separation bubble instabilities in hypersonic flow over a double wedge,” *J. Fluid Mech.* **941**, A7 (2022).
- G. Sidharth, A. Dwivedi, G. V. Candler, and J. W. Nichols, “Onset of three-dimensionality in supersonic flow over a slender double wedge,” *Phys. Rev. Fluids* **3**, 093901 (2018).
- J. Hao, J. Fan, S. Cao, and C. Wen, “Three-dimensionality of hypersonic laminar flow over a double cone,” *J. Fluid Mech.* **935**, A8 (2022).
- F. Li, M. M. Choudhari, P. Paredes, and A. Scholten, “Nonlinear evolution of instabilities in a laminar separation bubble at hypersonic Mach number,” in *AIAA AVIATION Forum* (AIAA, 2022), p. 3855.
- M. S. Holden, “Experimental studies of laminar separated flows induced by shock wave/boundary layer and shock/shock interaction in hypersonic flows for CFD validation,” in *AIAA 38th Aerospace Sciences Meeting and Exhibit* (AIAA, 2000), p. 0930.
- M. S. Holden, T. P. Wadhams, and M. G. MacLean, “Measurements in regions of shock wave/turbulent boundary layer interaction from Mach 4 to 10 for open and ‘blind’ code evaluation/validation,” in *21st AIAA Computational Fluid Dynamics Conference* (AIAA, 2013), p. 2836.

- <sup>21</sup>J. Fan, J. Hao, C. Wen, and X. Xue, “Numerical investigation of supersonic flow over a parachute-like configuration including turbulent flow effects,” *Aerosp. Sci. Technol.* **121**, 107330 (2022).
- <sup>22</sup>J. Fan, J. Hao, C. Wen, and X. Xue, “Unsteady supersonic flows past two-body configurations with different separation distances,” *J. Aerosp. Eng.* **36**(1), 04022109 (2023).
- <sup>23</sup>J. Hao, J. Wang, and C. Lee, “Numerical study of hypersonic flows over reentry configurations with different chemical nonequilibrium models,” *Acta Astronaut.* **126**, 1–10 (2016).
- <sup>24</sup>J. Hao and C. Wen, “Hypersonic flow over spherically blunted double cones,” *J. Fluid Mech.* **896**, A26 (2020).
- <sup>25</sup>Z. Chen, J. Hao, and C. Wen, “Control of supersonic compression corner flow using a plasma actuator,” *Phys. Fluids* **34**, 073605 (2022).
- <sup>26</sup>Q. Hong, J. Hao, C. K. Uy, C. Wen, and Q. Sun, “Thermochemical nonequilibrium effects on high-enthalpy double-wedge flows,” *Phys. Fluids* **34**, 063607 (2022).
- <sup>27</sup>R. W. MacCormack, *Numerical Computation of Compressible and Viscous Flow* (American Institute of Aeronautics and Astronautics, Inc., 2014).
- <sup>28</sup>B. Van Leer, “Towards the ultimate conservative difference scheme. II. Monotonicity and conservation combined in a second-order scheme,” *Comput. Phys.* **14**, 361–370 (1974).
- <sup>29</sup>D. M. Peterson, “Simulations of injection, mixing, and combustion in supersonic flow using a hybrid RANS/LES approach,” Ph.D. thesis (The University of Minnesota, 2011).
- <sup>30</sup>I. Nompelis, G. V. Candler, and M. S. Holden, “Effect of vibrational nonequilibrium on hypersonic double-cone experiments,” *AIAA J.* **41**(11), 2162–2169 (2003).
- <sup>31</sup>P. J. Schmid, “Dynamic mode decomposition of numerical and experimental data,” *J. Fluid Mech.* **656**, 5–28 (2010).
- <sup>32</sup>W. B. Collis, P. R. White, and J. K. Hammond, “Higher-order spectra: The bispectrum and trispectrum,” *Mech. Syst. Signal Process.* **12**, 375–394 (1998).
- <sup>33</sup>P. Welch, “The use of fast Fourier transform for the estimation of power spectra: A method based on time averaging over short, modified periodograms,” *IEEE Trans. Audio Electroacoust.* **15**, 70–73 (1967).
- <sup>34</sup>C. W. Rowley, I. Mezi, S. Bagheri, P. Schlatter, and D. S. Henningson, “Spectral analysis of nonlinear flows,” *J. Fluid Mech.* **641**, 115–128 (2009).
- <sup>35</sup>M. Jovanović, P. Schmid, and J. Nichols, “Sparsity-promoting dynamic mode decomposition,” *Phys. Fluids* **26**, 024103 (2014).
- <sup>36</sup>V. Pasquariello, S. Hickel, and N. A. Adams, “Unsteady effects of strong shock-wave/boundary-layer interaction at high Reynolds number,” *J. Fluid Mech.* **823**, 617–657 (2017).
- <sup>37</sup>S. Pirozzoli, J. Larsson, J. W. Nichols, M. Bernardini, B. E. Morgan, and S. K. Lele, *Analysis of Unsteady Effects in Shock/Boundary Layer Interactions* (CTR Summer Program, 2010).
- <sup>38</sup>A. Dwivedi, G. Sidharth, J. W. Nichols, G. V. Candler, and M. R. Jovanović, “Reattachment streaks in hypersonic compression ramp flow: An input-output analysis,” *J. Fluid Mech.* **880**, 113–135 (2019).
- <sup>39</sup>A. Dwivedi, N. Hildebrand, J. W. Nichols, G. V. Candler, and M. R. Jovanović, “Transient growth analysis of oblique shock-wave/boundary-layer interactions at Mach 5.92,” *Phys. Rev. Fluids* **5**, 063904 (2020).
- <sup>40</sup>A. Dwivedi, G. Sidharth, and M. Jovanović, “Oblique transition in hypersonic double-wedge flow,” *J. Fluid Mech.* **948**, A37 (2022).
- <sup>41</sup>M. Lugin, S. Beneddine, C. Leclercq, E. Garnier, and R. Bur, “Transition scenario in hypersonic axisymmetrical compression ramp flow,” *J. Fluid Mech.* **907**, A6 (2021).
- <sup>42</sup>B. Bugeat, J. C. Chassaing, J. C. Robinet, and P. Sagaut, “3D global optimal forcing and response of the supersonic boundary layer,” *J. Comput. Phys.* **398**, 108888 (2019).
- <sup>43</sup>B. Bugeat, J. C. Robinet, J. C. Chassaing, and P. Sagaut, “Low-frequency resolvent analysis of the laminar oblique shock wave/boundary layer interaction,” *J. Fluid Mech.* **942**, A43 (2022).
- <sup>44</sup>M. S. Loginov, N. A. Adams, and A. A. Zheltovodov, “Large-eddy simulation of shock-wave/turbulent-boundary-layer interaction,” *J. Fluid Mech.* **565**, 135–169 (2006).
- <sup>45</sup>S. Priebe, J. H. Tu, C. W. Rowley, and M. P. Martín, “Low-frequency dynamics in a shock-induced separated flow,” *J. Fluid Mech.* **807**, 441–477 (2016).
- <sup>46</sup>L. Agostini, L. Larchevêque, and P. Dupont, “Mechanism of shock unsteadiness in separated shock/boundary-layer interactions,” *Phys. Fluids* **27**, 126103 (2015).
- <sup>47</sup>K. M. Portera and J. Poggie, “Selective upstream influence on the unsteadiness of a separated turbulent compression ramp flow,” *Phys. Fluids* **31**, 016104 (2019).
- <sup>48</sup>J. Duan, X. Li, X. Li, and H. Liu, “Direct numerical simulation of a supersonic turbulent boundary layer over a compression–decompression corner,” *Phys. Fluids* **33**(6), 065111 (2021).
- <sup>49</sup>F. Tong, X. Yuan, J. Lai, J. Duan, D. Sun, and S. Dong, “Wall heat flux in a supersonic shock wave/turbulent boundary layer interaction,” *Phys. Fluids* **34**, 065104 (2022).
- <sup>50</sup>J. Zhang, T. Guo, G. Dang, and X. Li, “Direct numerical simulation of shock wave/turbulent boundary layer interaction in a swept compression ramp at Mach 6,” *Phys. Fluids* **34**, 116110 (2022).